

Study of the plutino object (208996) 2003 AZ₈₄ from stellar occultations: size, shape and topographic features

Dias-Oliveira, A.¹, Sicardy, B.², Ortiz, J. L.³, Braga-Ribas, F.^{4,1}, Leiva, R.^{2,5}, Vieira-Martins, R.^{1,6,7}, Benedetti-Rossi, G.¹, Camargo, J. I. B.^{1,7}, Assafin, M.⁸, Gomes-Júnior, A. R.⁸, Baug, T.⁹, Chandrasekhar, T.⁹, Desmars, J.², Duffard, R.³, Santos-Sanz, P.³, Ergang, Z.¹⁰, Ganesh, S.⁹, Ikari, Y.¹¹, Irawati, P.¹², Jain, J.⁹, Liying, Z.¹⁰, Richichi, A.¹², Shengbang, Q.¹⁰, Behrend, R.¹³, Benkhaldoun, Z.¹⁴, Brosch, N.¹⁵, Daassou, A.¹⁴, Frappa, E.¹⁶, Gal-Yam, A.¹⁷, Garcia-Lozano, R.¹⁸, Gillon, M.¹⁹, Jehin, E.¹⁹, Kaspi, S.¹⁵, Klotz, A.²⁰, Lecacheux, J.², Mahasena, P.²¹, Manfroid, J.¹⁹, Manulis, I.¹⁷, Maury, A.²², Mohan, V.²³, Morales, N.³, Ofek, E.¹⁷, Rinner, C.²⁴, Sharma, A.²⁵, Sposetti, S.¹³, Tanga, P.²⁶, Thirouin, A.²⁷, Vachier, F.⁶, Widemann, T.², Asai, A.¹¹, Watanabe, Hayato¹¹, Watanabe, Hiroyuki¹¹, Owada, M.¹¹, Yamamura, H.¹¹, Hayamizu, T.¹¹, Bradshaw, J.^{28,29}, Kerr, S.³⁰, Tomioka, H.³¹, Andersson, S.³², Dangl, G.³³, Haymes, T.³⁴, Naves, R.³⁵, Wortmann, G.³⁵

alexoliveira@on.br

oliveira.astro@gmail.com

-
- ¹Observatório Nacional/MCTI, Rua General José Cristino 77, Rio de Janeiro - RJ, 20.921-400, Brazil
- ²LESIA/Observatoire de Paris, CNRS UMR 8109, Université Pierre et Marie Curie, Université Paris-Diderot, 5 place Jules Janssen, F-92195 Meudon Cédex, France.
- ³Instituto de Astrofísica de Andalucía-CSIC, Apt 3004, 18080, Granada, Spain
- ⁴Federal University of Technology - Paraná (UTFPR / DAFIS), R. Sete de Setembro 3165, Curitiba - PR, 80230-901, Brazil
- ⁵Instituto de Astrofísica, Facultad de Física, Pontificia Universidad Católica de Chile, Av. Vicuña Mackenna 4860, 7820436 Macul, Santiago, Chile
- ⁶IMCCE/Observatoire de Paris, 77 Avenue Denfert Rochereau, Paris, 75014, France
- ⁷Laboratório Interinstitucional de e-Astronomia - LIneA, Rua General José Cristino 77, Rio de Janeiro - RJ, 20.921-400, Brazil
- ⁸Observatório do Valongo/UFRJ, Ladeira Pedro Antonio 43, Rio de Janeiro - RJ, 20080-090, Brazil
- ⁹Physical Research Laboratory, Ahmedabad, Gujarat 380009, India
- ¹⁰Yunnan Observatories, Chinese Academy of Sciences, Yunnan, China
- ¹¹Japan Occultation Information Network (JOIN), Japan
- ¹²National Astronomical Research Institute of Thailand, Siriphanich Building, Chiang Mai 50200 - Thailand
- ¹³Observatoire de Genève, 1290 Versoix, Switzerland
- ¹⁴Oukaimeden Observatory, LPHEA, Cadi Ayyad University, Marroch
- ¹⁵Wise Observatory and School of Physics and Astronomy, Tel-Aviv University, Tel-Aviv 69978, Israel
- ¹⁶EURASTER, 8 route de Soulomes, 46240 Labastide-Murat, France
- ¹⁷Department of Particle Physics and Astrophysics, Weizmann Institute of Science, Rehovot 7610001, Israel
- ¹⁸Observatorio de Busot, Spain
- ¹⁹Institut d'Astrophysique, de Géophysique et Océanographie, Université de Liège, Allée du 6 août 17, 4000 Liège, Belgium
- ²⁰Université de Toulouse, UPS-OMP, IRAP, 14 Avenue Edouard Belin, 31400 Toulouse, France
- ²¹Observatorium Bosscha, Institut Teknologi Bandung, Indonesia
- ²²San Pedro de Atacama Celestial Explorations (S.P.A.C.E.), San Pedro de Atacama, Chile
- ²³IUCAA Girawali Observatory, India
- ²⁴Moroccan Oukaimeden Sky Survey, Marroch
- ²⁵Nikaya Observatory, Tamil Nadu 635114, India
- ²⁶Laboratoire Lagrange, UMR7293, Uni. Côte d'Azur, CNRS, Observatoire de la Côte d'Azur Boulevard de l'Observatoire, CS 34229, 06304 Nice, France
- ²⁷Lowell Observatory, 1400 W Mars Hill Rd, Flagstaff, Arizona, United States of America
- ²⁸International Occultation Timing Association (IOTA), PO Box 7152, Kent, WA 98042, USA
- ²⁹Samford Valley Observatory, QLD, Australia
- ³⁰Royal Astronomical Society of New Zealand - Occultation Section
- ³¹Independent Astronomer
- ³²Amateursternwarte Mueggelheim, Wiesbacher Weg 8 , 12559 Berlin, Germany
- ³³A-3830, Nonndorf 12, Austria
- ³⁴BAA Asteroids and Remote Planets Section, Hill Rise, Knowl Hill Common, RG10 9YD, UK

ABSTRACT

We present results derived from four stellar occultations by the plutino object (208996) 2003 AZ₈₄, detected at January 8, 2011 (single-chord event), February 3, 2012 (multi-chord), December 2, 2013 (single-chord) and November 15, 2014 (multi-chord). Our observations rule out an oblate spheroid solution for 2003 AZ₈₄'s shape. Instead, assuming hydrostatic equilibrium, we find that a Jacobi triaxial solution with semi axes $(470 \pm 20) \times (383 \pm 10) \times (245 \pm 8)$ km can better account for all our occultation observations. Combining these dimensions with the rotation period of the body (6.75 h) and the amplitude of its rotation light curve, we derive a density $\rho = 0.87 \pm 0.01$ g cm⁻³ a geometric albedo $p_V = 0.097 \pm 0.009$. A grazing chord observed during the 2014 occultation reveals a topographic feature along 2003 AZ₈₄'s limb, that can be interpreted as an abrupt chasm of width ~ 23 km and depth > 8 km or a smooth depression of width ~ 80 km and depth ~ 13 km (or an intermediate feature between those two extremes).

Subject headings: Kuiper belt objects: individual (208996, 2003 AZ₈₄) - occultations - planets and satellites: surfaces - planets and satellites: fundamental parameters

1. INTRODUCTION

The size, mass, shape, albedo, chemical composition and orbital elements distribution of the Trans-Neptunian Objects (TNOs) provide important information on the chemical and dynamical evolution of our Solar System (Lykawka & Mukai 2008). In addition, as their surfaces are little affected by solar radiation due to their large heliocentric distances, they give us clues to the composition of the primordial nebula. Unfortunately, the faintness and small angular sizes of most of them, make their study difficult, so that our knowledge of these objects remains fragmentary (Stansberry et al. 2008).

One of the most effective techniques to study these bodies is the stellar occultation method, which can provide sizes and shapes down to km-level accuracy, reveal atmospheres at the few nbar level (Sicardy et al. (2011); Ortiz et al. (2012)), and detect features like jets, satellites and rings (Braga-Ribas et al. 2014a; Ortiz et al. 2015; Ruprecht et al. 2015).

Besides Pluto and Charon, since 2009, after the first successful observation of a stellar occultation by the TNO 2002 TX₃₀₀, see Elliot et al. (2010), several objects have been measured by stellar occultations, like Varuna (Sicardy et al. 2010), Eris (Sicardy et al. 2011), Quaoar (Person et al. 2011, Sallum et al. 2011, Braga-Ribas et al. 2013), Makemake (Ortiz et al. 2012), 2002 KX₁₄ (Alvarez-Candal et al. 2014) and 2007 UK₁₂₆ (Benedetti-Rossi et al. 2016).

Adding to the list above, we now have (208996) 2003 AZ₈₄, a large TNO classified as a plutino (object in the 3:2 mean motion resonance with Neptune) (Marsden, et al. 2009). It was discovered in January 2003 by Trujillo et al. (2003) and has an estimated area-equivalent radius and visible geometric albedo of 364_{-33}^{+31} km and $0.107_{-0.016}^{+0.023}$, respectively, as derived from thermal measurements (Mommert et al. 2012). Its orbit has a semi-major axis of 39.406 AU, aphelion distance 46.477 AU, orbital period 247.37 yr, orbital eccentricity

³⁵c/Jaume Balmes n 24 Cabrils 08348, Spain

³⁶Archenhold-Observatory, Neue Krugallee 180, D-12437 Berlin, Germany

0.179 and inclination of 13.563 degrees¹. It also has a satellite fainter than the primary by 5.0 ± 0.3 mag (Brown and Suer 2007) located at a typical distance of 10,000 km from the primary. However, due to lack of data, its orbit is still unknown and no mass estimate for the system has been derived.

We present here four stellar occultations by 2003 AZ₈₄. The first one ever observed involving this body was a single-chord event detected on January 8, 2011 in Chile, while another single-chord occultation was observed on December 2, 2013 in Australia. Both events provide lower limits for the semi-major axis of the object, as discussed ahead in the main text.

On the other hand, multi-chord events were observed on February 3, 2012 and on November 15, 2014. The 2012 event was detected from three sites, two in India and one in Israel. The November 15, 2014 event was recorded from sites in China, Thailand and Japan. The latter provides the best signal-to-noise ratio and time resolution light curves of all four events. Moreover, the China observation shows a gradual star disappearance that is better fitted as a topographic feature at the surface of the body. This is the first solid report of of this kind from a stellar occultation by a TNO.

The occultation prediction methods are outlined in Section 2. Data analysis is presented in Section 3 and results are given in Section 4 (in particular on the size and shape of the body and on the presence of a topographic feature), before concluding remarks in Section 5.

2. PREDICTIONS AND OBSERVATIONS

Considering the importance of TNO occultations and the challenges they pose (essentially due to the high degree of accuracy required on the TNO orbit and star position), huge efforts were dedicated to the prediction of the events described here. The candidate stars were identified in systematic surveys performed at the 2.2 m telescope of the European Southern Observatory (ESO) at La Silla, using the Wide Field Imager (WFI). The surveys yielded local astrometric catalogues for 5 Centaurs and 34 TNOs (plus Pluto and its moons) up to 2015, with stars with magnitudes as faint as $R_{\text{mag}} \sim 19$ mag (Assafin et al. 2010, 2012; Camargo et al. 2014). Close to the occultation dates, astrometric updates of the candidate stars (and if possible, the TNO) were performed to improve the predictions by avoiding systematic biases, like catalog errors.

The updates for the February 3, 2012 event were based on observations carried out between September 22, 2011 and January 25, 2012 (Table 1). Those measurements confirmed that the shadow’s path should pass across North Africa and Middle East. They provide the following ICRF/J2000 star position:

$$\begin{aligned}\alpha &= 07^{\text{h}}45^{\text{m}}54.7696^{\text{s}} \pm 0.022'' \\ \delta &= +11^{\circ}12'43.093'' \pm 0.023'',\end{aligned}\tag{1}$$

For the November 15, 2014 event, we used the Version 1 of NIMA ephemeris² (NIMA V1 hereafter) to get a short period correction for 2003 AZ₈₄’s motion, using previous observations. NIMA determines and propagates the orbit through the numerical integration of the equations of motion, based on the least squares method to iteratively find the corrections to

¹<http://ssd.jpl.nasa.gov/sbdb.cgi?sstr=2003AZ84>

²Numerical Integration of the Motion of an Asteroid, see <http://josselin.desmars.free.fr/tno/2003AZ84>

each component of the state vector from observations. Compared to JPL ephemeris, we used additional observations from Pic du Midi and ESO, two astrometric positions deduced from positive occultations on 8 January 2011 and 3, February 2012, and a specific weighting scheme depending on the observatory, the stellar catalogue used for the reduction, and the number of observations per night (see Desmars et al. 2015 for more details). The ephemeris, with average standard deviations of 40 milli-arcsec (mas) with respect to observations, was combined with astrometric observations of the candidate star, carried out with the two 0.60 m telescopes (Zeiss and Boller and Chivens) at Pico dos Dias Observatory in Brazil (IAU code 874), providing the following ICRF/J2000 star position:

$$\begin{aligned}\alpha &= 08^{\text{h}}03^{\text{m}}51.2980^{\text{s}} \pm 0.022'' \\ \delta &= +09^{\circ}57'18.729'' \pm 0.023''\end{aligned}\tag{2}$$

The combination confirmed a shadow path going over Japan, Thailand and part of China, leading us to trigger alerts at several potential sites shown in Fig. 1. The circumstances of observations for both 2012 and 2014 events are listed in Tables 2 and 3.

3. DATA ANALYSIS

3.1. OCCULTATION LIGHT CURVES

For the events described below, the flux from the star (plus the faint, background contribution due to the occulting body) was obtained through differential aperture photometry using the PRAIA package (Assafin et al. 2011). The resulting light-curve (flux vs. time) was then normalized to its unocculted value, using polynomial fits – first or third degree depending on the data quality – to the flux before and after the event.

3.1.1. *Single-Chord events 2011 and 2013*

The single chord occultation of January 8, 2011 had a typical shadow velocity of 26 km s^{-1} . It was observed at San Pedro de Atacama Celestial Explorations Observatory (longitude $68^{\circ} 10' 48.70''$ W, latitude $22^{\circ} 57' 09.80''$ S, altitude 2400 m) in Chile, by Alain Maury using the C. Harlinton 0.5-m Planewave telescope (Fig. 3) and by Nicolas Morales with the remotely operated 0.4-m ASH2 telescope. On the other hand, the single chord event of December 2, 2013 had a shadow velocity of about 17 km s^{-1} and was observed by Steve Kerr, near Rockhampton (longitude $150^{\circ} 30' 00.80''$ E, latitude $23^{\circ} 16' 09.60''$ S, altitude 50 m) in Australia. The event was recorded with a Watec 120N+ video camera attached to a 0.30 m telescope attached, with cycle 2.56 s exposure time.

The occultation durations (see Fig. 3 and Table 4) corresponds to chord lengths of $573 \pm 21 \text{ km}$ and $657 \pm 35 \text{ km}$ for the 2011 and 2013 events, respectively and provide lower limits for the major-axis of the object (Braga-Ribas et al. 2011; Braga-Ribas et al. 2014b).

3.1.2. *February 3, 2012*

Three occulting sites recorded this event, Mount Abu Observatory and IUCAA (Inter-University Centre for Astronomy and Astrophysics) Girawali Observatory in India, plus the Kraar Observatory in Israel. The

event had a typical shadow velocity of 25 km s^{-1} , see details in Table 2.

Although all the sites had robust clock synchronizations, the acquisition software used for all of them recorded only the integer part of the second in each image header. In order to retrieve the fractional part of the second for the mid-exposure time t_i of each image i , we performed linear fits to the set (i, t_i) as used by Sicardy et al. (2011).

The residuals of this linear fit show a saw pattern with dispersion between -0.5 and $+0.5$ seconds (Fig. 2 for example), showing that there is truncation and the period in which the acquisition cycle is regular. From this fit we obtain the acquisition cycle t_c , which is used to obtain the time of each image t_{fit} , now with the fraction of the second, and an initial time t_0 (Eq. 3).

$$t_{fit} = t_0 + (t_c \cdot i) + 0.5 \quad (3)$$

Half a second is added to the times to correct the offset imposed by the truncation. With this procedure the times of each image have an internal precision that depends on the square root of the number of images used and is less than one second. In the present case, we could retrieve the individual times t_{fit} to within an accuracy of 0.06 s .

Note that the IUCAA light curve was obtained with an exposure time of 2 s , and a long read-out time of 14.5 s which provides a single occultation point with partial flux drop, and a large uncertainty on the ingress time at that station, see discussion below, Table 4 and Fig. 6.

3.1.3. November 15, 2014

This event was the slowest of all described here, with a shadow velocity of about 9.4 km s^{-1} . Four light curves were obtained at three different sites: the Yunnan station in China, the Thai National Telescope (TNT) in Thailand and the Moriyama station in Japan, see Table 3 and Fig. 4. For the three CCD recordings, the mid-exposure times t_i were extracted from the image headers. The headers from the Thai National Telescope images provide t_i down to the millisecond while for both the Yunnan and Moriyama images, only the integer part of the second was recorded, thus requiring the same procedure as described in the previous subsection.

The Moriyama site also recorded the event with a video camera attached to a 25.4 cm telescope. The data were collected by integrating 256 video frames to provide a complete exposure of approximately 8 s , with GPS time inserted in each frame. Using the Audela software³, we extracted individual frames in FITS format from the video. This conversion process requires special care because of possible dropped frames, duplicated fields or any software incompatibility (Buie & Keller 2016). Because of that, detailed checks were performed in all sets of images to ensure that the extracted time corresponds to the time printed at each frame.

Also, AUDELA conversion software create a FITS image for each video frame, instead of for each

³a free and open source astronomy software for digital observations: CCD cameras, Web cams, etc..., see <http://audela.org/dokuwiki/doku.php?id=en:start>

exposure. So, it is important to check exactly how many of the exported FITS frames belong to a single acquisition, in order to combine them properly into a single image. Using photometry and observing the step-like variations of the target brightness, we can identify in each step the 256 frames that represent a single acquisition and that must be averaged out.

More precisely, in order to avoid taking into account any field from the previous or next acquisition, we excluded the first and last frame from a sequence, and then averaged out the remaining 254 frames. To ensure a correct time-stamping of each final images, we used the mid-exposure time of the mid-frame of each sequence.

A noteworthy feature observed during this occultation is the gradual decrease of the stellar flux observed over three acquisition intervals during the star disappearance at the Yunnan site (Fig. 5). This feature is analyzed in more detail below and was interpreted as a topographic feature. Note that this effect cannot be the result of photometric noise, as the typical photometric error of each data point is about 0.0236 mag, less than 6% of the observed flux variation, thus ruling out photometric problems. Moreover, a careful visual analysis of the three corresponding images clearly shows a gradual disappearance of the star, without any similar behavior for the other reference objects acquired in the field of view.

3.2. OCCULTATION TIMING

To determine the start and end times of the occultation we fitted for each light curve a sharp edge occultation model convolved by Fresnel diffraction, CCD bandwidth, stellar diameter projected at the body and finite integration time, see Widemann et al. (2009); Braga-Ribas et al. (2013).

With 2003 AZ₈₄'s geocentric distances of $D = 44.3$ AU in 2012 and $D = 44.5$ AU in 2014, the Fresnel scale ($F = \sqrt{\lambda D/2}$) for a typical wavelength of $\lambda = 0.65 \mu\text{m}$ (and $\lambda = 1.65 \mu\text{m}$ for Mt. Abu) is derived for each event, $F = 1.47$ km (2.34 km for Mt. Abu) in 2012, and $F = 1.46$ km in 2014.

The star diameter projected at 2003 AZ₈₄'s distance was estimated using the B , V and K apparent magnitudes provided by the NOMAD catalogue (Zacharias et al. 2004) and the formulae of van Belle (1999). The 2012 star ($B = 15.8$ mag, $V = 15.35$ mag, $K = 14.1$ mag) has then an estimated projected diameter of 0.24 km, while it is 0.20 km for the 2014 star ($B = 15.5$ mag, $V = 15.5$ mag and $K = 14.0$ mag).

Using the apparent TNO motion relative to the star, it is possible to translate the integration times into actual distances traveled in the sky plane. The smallest integration times were 2.0 s in 2012 and 0.786 s in 2014, corresponding to 49.7 km and 7.50 km in the celestial plane, respectively. Therefore, our light curves are dominated by the integration times, and not by Fresnel diffraction or stellar diameter. The same is true for the 2011 and 2013 events.

The free parameters to adjust in the fits are the times t_{occ} of ingress (star disappearance) or egress (star re-appearance) for each station. The value of t_{occ} is obtained by minimizing a classical χ^2 function, as described in Sicardy et al. (2011). The resulting best fits are shown in Fig. 6, and the occultation times are listed in Table 4.

The IUCAA light curve is special, however, because it has only one data point with a partial drop of the stellar flux (Fig. 6), meaning that the star was occulted during a fraction of this 2-s acquisition interval. Calibration data taken with the same instrument on February 10, 2012 provide the separate fluxes of 2003 AZ₈₄ and the star, allowing us to estimate the fraction of time when the star was occulted during

that interval. Note that from the light curve, we cannot discriminate between an ingress or egress point. However, considering the location of the point in the sky plane and comparing it to the other chords, it seems more likely to be an egress point, with an ingress that happened during 14.5 s gap between the end of the previous exposure, and before the start of the current exposure. The alternative solution (with egress happening during the gap after the single drop) would result in a very elongated body which is unlikely, see Fig. 6.

3.3. LIMB FITTING

The ingress and egress times t_{occ} provide the positions of the star in the sky plane relative to 2003 AZ₈₄'s center, once the star position is specified (Eqs. 2 and 3), and for a given ephemeris (NIMA V1 in our case). More precisely, each timing gives the position (f, g) of the star with respect to the body center, f and g being measured positively towards local celestial east and celestial north, respectively.

For each event, the general shape for the body's limb was assumed to be an ellipse characterized by $M = 5$ adjustable parameters: the coordinates of the ellipse center, (f_c, g_c) ; the apparent semi-major axis a' ; the apparent oblateness $\epsilon' = (a' - b')/a'$ (where b' is the apparent semi-minor axis) and **the position angle of the pole P_p of b' , which is the geocentric position angle of the pole measured eastward from the north.** Note that the center (f_c, g_c) actually measures the offsets in right ascension and declination to be applied to the ephemeris in use, assuming that the star position is correct. Note also that the quantities a' , b' , f_c and g_c are all expressed in kilometers.

The ingress and egress times from each light curve provides the extremities of the corresponding occultation chord. As both ingress and egress times from Moriyama's light curves agree at 1- σ level, we consider only one chord for that station (the one obtained with CCD) for the limb fitting. Thus, for each event there are three positive observations, providing $N = 6$ chord extremities (ingress and egress), with positions $f_{i,obs}$, $g_{i,obs}$ (Fig. 6 and 7). The best elliptical fit to the chord extremities is found by minimizing the relevant χ^2 function (see e.g. Sicardy et al. 2011). In that case, the statistical significance of the fit is evaluated from the χ^2 per degree of freedom (pdf) defined as $\chi_{\text{pdf}}^2 = \chi^2/(N - M)$, which should be close to unity. **The individual 1- σ error bar of each parameter is obtained by varying manually the given parameter from its nominal solution value (keeping the other ones fixed) so that χ^2 varies from its minimum value χ_{min}^2 to $\chi_{\text{min}}^2 + 1$.**

4. RESULTS

4.1. LIMB FITTINGS TO THE 2012 AND 2014 EVENTS

The parameters of the best elliptical fits for the 2012 and 2014 events are given in Table 5, which provides the shapes of the limb and the offsets to be applied to the used ephemeris. Those fits clearly show a change in the limb shape between those two dates, see Figs. 6 and 7. This said, the fits provide best values of $\chi_{\text{pdf}}^2 = 0.73$ (2012) and $\chi_{\text{pdf}}^2 = 0.98$ (2014), which indicates satisfactory fits.

The main change concerns to the apparent oblateness of the body that varies from $\epsilon' = 0.340_{-0.086}^{+0.097}$ in 2012 to $\epsilon' = 0.054 \pm 0.003$ in 2014, with a difference of more than 3- σ . Conversely, the apparent semi-major axes are $a = 426 \pm 20$ km (2012) and $a = 393 \pm 1$ km (2014), with a barely significant difference at 2- σ level. Note in passing that these results agree with the lower limits on the major-axis 573 ± 21 km and 657 ± 35 km

quoted earlier, derived from the single-chord events of 2011 and 2013 events. Similarly, the two fits provide consistent ($1\text{-}\sigma$ level) position angles of the limb: $P_L = 41^{\circ+8}_{-5}$ (2012) and $P_L = 36^{\circ} \pm 4^{\circ}$ (2014). The P_L is geocentric position angle of the northern semi-minor axis of the projected limb, measured eastward from the north. (not to be confounded with **position angle of the pole** P_p).

We may attribute the change of the retrieved ϵ' to a very irregular shape, but reconciling the limbs of Figs. 6 and 7 at face values would require topographic features of up to 40 km above an average elliptical limb. Hydrostatic equilibrium is expected for objects with diameter on the order of 1000 km. More precisely, the critical diameter necessary to reach equilibrium for bodies with slow rotation may vary between 500–1200 km for rocky bodies, and between 200–900 km for icy bodies (Tancredi & Favre 2008). In this context, the body assumes either the shape of a Jacobi ellipsoid with principal axes $a > b > c$ or that of a Maclaurin spheroid $a = b > c$, depending on their angular momentum (Chandrasekhar 1987).

Assuming first a Maclaurin solution, the variation of ϵ' between 2012 and 2014 could in principle be caused by a variation with time of the opening angle⁴ B due to a mere change of viewing geometry. The true oblateness $\epsilon = 1 - (c/a)$ is related to the apparent oblateness through $\epsilon' = 1 - \sqrt{\sin^2(B) + (1 - \epsilon)^2 \cos^2(B)}$, and it is easy to see that the larger ϵ , the smaller the change of B necessary to change ϵ' by a given amount. As the Maclaurin solutions have $\epsilon < 0.417$ (Tancredi & Favre 2008), it results that changing ϵ' from $0.340^{+0.097}_{-0.086}$ to 0.054 ± 0.003 requires changing of B by at least 45^{+20}_{-15} degrees. This cannot be caused just by a variable viewing geometry, because of the large geocentric distance of 2003 AZ₈₄ (more than 43 AU) and of its slow heliocentric motion. In fact, testing a set of random pole positions, the maximum difference in B between 2012 and 2014 is found to be less than ~ 5 degrees.

An alternative explanation for a changing B is a precession caused by the solar torque on 2003 AZ₈₄. Classical calculations (e.g. Goldstein 1950) provide a precession rate of $-3GM_{\odot}/(2r^3\omega)\epsilon \cos(\theta)$ for a spheroid, where G is the constant of gravitation, M_{\odot} and r are the Sun mass and distance, respectively, ω is the spin frequency, and θ is the obliquity. At $r > 43$ AU and with a rotation period of 6.75 ± 0.04 h (Thirouin et al. 2010), we have $3GM_{\odot}/(2r^3\omega) \sim 10^{-15}$ rad s⁻¹, far too small to explain any significant change of pole orientation in only two years.

The same conclusion follows if the precession is caused by the satellite reported by Brown and Suer (2007). From the numbers quoted in the Introduction, and assuming same albedos, the satellite should have a typical radius of 40 km, corresponding to a mass M of a few times 10^{17} kg for an icy composition. This implies $3GM/(2r^3\omega) \sim 10^{-10}$ rad s⁻¹ (taking $r \sim 10,000$ km), still too small for explaining any significant changes of the pole orientation in two years.

Finally, the object aspect angle might change due to a misalignment between 2003 AZ₈₄'s angular momentum and its minor axis, causing a wobbling, for instance as a consequence of a collision. Burns & Mukai (1973) estimated alignment times for typical small bodies from 4 to 200 km in radius, and found typical times from $\sim 6 \times 10^7$ to $\sim 10^5$ yr, respectively. Therefore, for 2003 AZ₈₄, the alignment time should be very short ($< 10^5$ years), making the wobbling hypothesis highly unlikely. At this point, we are left with the Jacobi shape alternative, which is explored in more details in the next section.

⁴The angle between the line of sight and the equatorial plane of the body, with $B = 0^{\circ}$ (resp. $B = 90^{\circ}$) corresponding to the equator-on (resp. pole-on) geometry. It is sometimes referred to as the observer planetocentric elevation and is related to the polar aspect angle ξ through $B = 90^{\circ} - \xi$.

4.2. JACOBI SOLUTION

Here, we look for a unique Jacobi body with fixed pole position that can account for both 2012 and 2014 occultations (Figs. 6 and 7). A second condition that we impose is that this solution is also compatible with the (single peaked) amplitude of 2003 AZ₈₄'s rotational light curve, $\Delta m = 0.07 \pm 0.01$ mag reported by Thirouin et al. (2010); Ortiz et al. (2006).

For a stable Jacobi ellipsoid, the adimensional quantity $\Omega = \omega^2/(G\pi\rho)$ is bounded between 0.284 and 0.374 (Chandrasekhar 1987). If we assume that the body is a triaxial ellipsoid, the full rotation period should actually be $6.75 \times 2 = 13.5$ h. This would imply, from the definition of Ω , that the density lies in the interval $0.21 < \rho < 0.28$ g cm⁻³, unrealistic low values for ρ . If we adopt a rotational period of 6.75 h (thus assuming that the rotational light curve is caused by albedo features, not by shape effects, see discussion below), then the density is restricted to the interval $0.85 < \rho < 1.12$ g cm⁻³.

Now, for each value of ρ , there is a unique Jacobi ellipsoid solution, and more precisely unique ratios b/a and c/b , where $a > b > c$ are the principal axes of the body. We simplify the problem further by assuming that the object does not change its pole orientation relative to the observer between the 2012 and 2014 occultations. In this way, the changes of its limb shape are solely due to the rotation around the pole axis. As commented before, exploring random pole orientations, the maximum difference in B between 2012 and 2014 is less than ~ 5 degrees, while the typical change in the position angle of the pole is ~ 7 degrees, making our assumption reasonable.

Then, we determine numerically a set of combinations of B and ρ for which there is a pair of rotation angle⁵ Q and common value of a that is compatible (to within error bars) with the projected sizes and oblatenesses ϵ' of both 2012 and 2014 events. Note that given the current accuracy on 2003 AZ₈₄'s rotation period (6.75 ± 0.04 h) and the interval of more than two years between the two observations, the corresponding values of Q are considered as uncorrelated between 2012 and 2014.

Next, for a set of densities ρ between 0.85 and 1.12 g cm⁻³, we consider the corresponding Jacobi solutions, with their associated ratios b/a and c/a . This constrains (ρ, B) to lie on a banded-shape domain that reflects the $1\text{-}\sigma$ uncertainties on the limb parameters, see the hatched region in Fig. 8. We note that near equator-on solutions ($B \sim 0^\circ$) are ruled out as they generate very elongated projected shapes, especially for low density ellipsoids, that are incompatible with the moderate apparent oblatenesses of Table 5 (and with the very small amplitude derived from the rotational light curve). On the other hand, near pole-on solutions ($B \sim 90^\circ$) are also ruled out as they generate little changes in projected oblateness whatever the value of Q is, while the oblatenesses between 2012 and 2014 are significantly different.

We now use the amplitude of the rotational lightcurve ($\Delta m = 0.07 \pm 0.01$ mag) as an independent constraint. Since the 6.75 h rotational light curve is single peaked, while we assume here a Jacobi shape, this means that the observed variability is caused by albedo features, not by the shape. In that context, we can only state that the Jacobi solution must be such that it causes variations of apparent cross section that have an amplitude smaller than 0.07 magnitude (Binzel et al. 1989) This defines another possible domain for (ρ, B) , see the gray band in Fig. 8. The intersection of the two domains puts a stringent constraint $\rho = 0.87 \pm 0.01$ g cm⁻³ for the density of the Jacobi body we are looking for, with axis ratios $b/a = 0.82 \pm 0.05$ and $c/a = 0.52 \pm 0.02$. Exploring the intersection domain shown in Fig. 8, we find that

⁵The rotation angle origin, $Q = 0$, is arbitrarily defined when the longer axis a points towards the observer and is counted positively following the right-hand rule around the pole axis.

Jacobi ellipsoids with a fixed pole orientation can fit both 2012 and 2014 limbs with a semi axes ranges of $a = 470 \pm 20$ km, $b = 383 \pm 10$ km and $c = 245 \pm 8$ km (1- σ level).

An example of a possible solution is given in Fig. 9, corresponding to $a = 456$ km, $\rho = 0.86$ g cm⁻³ and rotation angles $Q = 24^\circ$ (2012) and $Q = 10^\circ$ (2014). A full treatment that provides a global best fit and finer error bars would require a bayesian approach. This remains out of the scope of this paper, but our example shows that a unique Jacobi solution meeting all the constraints (our occultation results plus the rotational light curve amplitude) do exist in narrow intervals of ρ and a .

Finally, the intersection region in Fig. 8 provides a range for the equivalent radius of the body, $R_{\text{eq}} = 386 \pm 6$ km (as observed in 2012 and 2014), i.e. the radius of the disk that has the same apparent area as the observed body. Using this value, we obtain the geometric albedo in visible band through

$$p_V = (AU_{\text{km}}/R_{\text{eq}})^2 \times 10^{0.4(H_{\odot,V} - H_V)}, \quad (4)$$

where $AU_{\text{km}} = 1.49597870700 \times 10^8$ km, $H_{\odot,V} = -26.74$ mag is the Sun magnitude at 1 AU in the visible. From 2003 AZ₈₄'s visible absolute magnitude, $H_V = 3.74 \pm 0.09$ mag (Mommert et al. 2012), and the value R_{eq} obtained above, we derive $p_V = 0.097 \pm 0.009$.

4.3. TOPOGRAPHIC FEATURE

Fig. 5 shows the gradual disappearance of the star during ingress at the Yunnan station. It took more than 8 seconds for the stellar flux to go from its unocculted level to complete disappearance. This corresponds to a displacement of the stellar image of more than 80 km along the local limb. Since this is the only instance of gradual dimming observed during this event, it must come from a localized feature on the limb and cannot stem from a star duplicity. Various causes might explain this behavior, the most plausible one being a topographic feature revealed by the grazing geometry of the chord (Fig. 7).

Beyond a topographic origin, only exotic explanations may be envisaged, like the presence of a local dust cloud lingering over the surface, or a local atmosphere that refracts the stellar rays. The drops of signal observed during intervals A and B in Fig. 5 would imply average tangential optical depths of $\tau_A = 0.53$ and $\tau_B = 0.83$, respectively, for dusty material (assuming that point C is then be the usual star disappearance behind the solid limb). This would imply in a very dense local dusty cloud with length ~ 80 km and height ~ 10 km. An intense cometary-like activity would be required to create such cloud, an unlikely process so far away from the Sun (~ 45 AU), and such an activity has not been reported before for 2003 AZ₈₄.

On the other hand, Ortiz et al. (2012) analyzed the effects of a localized atmosphere during an occultation. Typical surface pressures of a few microbars are required to create the feature of Fig. 5. A stationary local atmosphere could result from a delicate balance between local sublimation and recondensation farther away on the surface. To analyze further this scenario, it is necessary to know the pole position of the object in order to determine the sub-solar latitude along the limb (where sublimation would be favored). Moreover, an albedo map of 2003 AZ₈₄ would be useful to identify warmer/cooler terrains where sublimation/condensation could be favored. These pieces of information are missing right now, preventing a more detailed discussion of the local atmosphere hypothesis.

Returning to the topographic feature explanation, we note that each integration interval lasts for 3 seconds (Table 3), corresponding to about 28 km traveled by the star parallel to the limb, while the complete duty cycle (4.3 s) corresponds to about 40 km. In that context, there is an infinity of solutions for the limb

structure that fit equally well the observed light curve. For instance, the star may disappear and re-appear several times behind local reliefs during a single acquisition interval.

We examine here two extreme, simple solutions that provide possible ranges for the width and depth of the limb feature. One solution (Solution 1) assumes that the observed light curve is caused by a chasm with vertical, abrupt walls (that is, perpendicular to the global fitted limb displayed in Fig. 7), while Solution 2 assumes that the topographic features is smooth with very shallow slopes, corresponding to a local limb that is always parallel to the global limb. In both solutions, we have to convolve the sharp shadow edge profile by the Fresnel diffraction pattern, the stellar diameter and the integration time. The Fresnel pattern corresponding to the November 15, 2014 event is displayed in Fig. 10. As the projected stellar diameter is estimated to be 0.2 km, it is negligible compared to the Fresnel scale, ~ 1.5 km (see Section 3.2). Thus the occultation light curve is dominated by Fresnel diffraction, and of course, by the large integration time (3 s) at the Yunnan station.

In the Solution 1 scenario, the star first disappears behind the global limb, then it re-appears in the chasm during interval B, and disappear again during interval C. During intervals D and E, the star is completely hidden behind the body, and it re-appears from behind the global limb near the start of interval F. The locations of the walls are then adjusted so as to reproduce the observed fluxes (Fig. 5).

Solution 2 is a bit more complex to implement, as the star velocity relative to the body center varies significantly during each acquisition interval. To generate a synthetic light curve, we calculate the position of the star relative to the body center at regular time steps of 0.1 second inside each integration interval (black dots in Fig. 11). Using the Fresnel pattern of Fig. 10, we can generate the synthetic flux by averaging the theoretical fluxes calculated at each 0.1 s step inside a given interval. The free parameter in this calculation is the radial offset of the local limb (corresponding to the blue lines in Fig. 10), adjusted so as to fit the observed profile. This offset provides in turn the difference between the positions of the local limb and that of the global limb (red lines in Fig. 11), and eventually the average elevation of the terrain in each interval (Fig. 12).

Fig. 13 summarizes our results. The first panel sketches our inferred chasm structure (Solution 1) with a width of 22.6 ± 0.4 km, while only a lower limit of about 8 km can be given for its depth. The second panel (Solution 2) reveals a general depression that reaches more than 13 km in depth and extends over more than 80 km along the limb.

These structures can be compared with topographic features recently revealed on Pluto’s and Charon’s surfaces during the New Horizons flyby (Stern et al. 2015; Nimmo et al. 2016). On both bodies, features reaching depths of up to 10 km are observed, some of them extending over tens of kilometers on the surface. This supports our finding of a chasm or depression on 2003 AZ₈₄’s surface, as this body is smaller (semi-major axis radius $a < 500$ km, see previous section) than Pluto and Charon (radii 1188 km and 606 km respectively, see Nimmo et al. 2016), and thus can in principle sustain comparable or deeper topographic features.

5. CONCLUSIONS

We have combined data from four stellar occultations by the plutino object 2003 AZ₈₄ observed in 2011 (January 8), 2012 (February 3), 2013 (December 2) and 2014 (November 15), two of them being single-chord (2011 and 2013) and the other two being multi-chord events (2012 and 2014).

The multi-chord events provide different limb shapes (Figs. 6 and 7) that we interpret as being due to a Jacobi ellipsoid that has been observed in 2012 and 2014 at two different rotation angles. This Jacobi solution has a semi-major axis $a = 470 \pm 20$ km, axis ratios $b/a = 0.82 \pm 0.05$ and $c/a = 0.52 \pm 0.02$ (corresponding to $b = 383 \pm 10$ km and $c = 245 \pm 8$ km) and density $\rho = 0.87 \pm 0.01$ g cm⁻³. The equivalent radius $R_{\text{eq}} = 386 \pm 6$ km that we derive for 2003 AZ₈₄ (in 2012 and 2014) provides a visible geometric albedo of $p_V = 0.097 \pm 0.009$. Both values are consistent with those derived from thermal measurements, $R_{\text{eq}} = 364_{-33}^{+31}$ km and $p_V = 0.107_{-0.016}^{+0.023}$ (Mommert et al. 2012), but with higher accuracy.

Besides yielding accurate sizes, these occultations also constrain the shape of the body. Some words of caution should be mentioned here, as we have only two multi-chord events at hand, and some unaccounted timing errors might be present in some of our data. Consequently, more occultations are now required to confirm our Jacobi solution. This said, we have devised a general method, summarized in Fig. 8, that combines several multi-chord occultations and the amplitude of rotation derived from ordinary light curves to eventually pin down (or rule out) a Jacobi solution for the body. This method can be employed for analyzing future occultations by 2003 AZ₈₄ and other TNOs. Note that as more observations are added, this method will put stringent constraints on the pole position, which in turn can be compared with the orientation of the satellite’s orbit, when available. The orbital period of the satellite will also provide 2003 AZ₈₄’s mass, which in turn can be compared with the mass derived from the occultations, as described above.

The shape and density of 2003 AZ₈₄ can be compared with that of other elongated TNOs like Haumea and Varuna, which have respective rotation periods of 3.9 h and 6.4 h (Thirouin et al. 2016; Mueller 2015). Using observed rotation light-curves, Lacerda & Jewitt (2007) infer values of $\rho \sim 2.6$ and $\rho \sim 1.0$ g cm⁻³ for Haumea’s and Varuna’s densities, respectively, with corresponding axis ratios ($b/a \sim 0.83, c/a \sim 0.53$) and ($b/a \sim 0.73, c/a \sim 0.49$) for each object. Thus, 2003 AZ₈₄ should resemble Haumea and Varuna in terms of shape, with a density that is close to that of Varuna, adding one more object to the family of very elongated TNOs.

Another noteworthy result obtained here is the detection of a topographic feature at the surface of 2003 AZ₈₄, a première if we exclude Pluto and Charon. Due to the lack of time resolution in our data, we cannot discriminate between an abrupt chasm of width ~ 23 km and depth > 8 km, a depression with shallow slopes, width of ~ 80 km and depth of ~ 13 km, or other intermediate solutions (Fig. 13). Again, more occultations are required to pin down the structure of this kind of features. Note, however, that gradual star dis- or re-appearances occur if the occultation chord is at less than typically 10 km from the average limb of the body. In the Gaia era, star positions will be given at accuracies better than 1 mas. In this context, successful occultations will themselves improve the ephemeris of the body, eventually providing predictions of new occultations with accuracies as good as ~ 1 mas. This corresponds to about 30 km at 2003 AZ₈₄’s distance, or about 10 km for typical Centaur objects. This will turn grazing occultations by remote bodies from a hopeless task to a routine method that will reveal rims, chasm, craters (with irregular edges), basins, etc..., thus fostering geological studies of those objects.

Acknowledgments. We acknowledge support from the French grants “Beyond Neptune” ANR-08-BLAN-0177 and “Beyond Neptune II” ANR-11-IS56-0002. Part of the research leading to these results has received funding from the European Research Council under the European Community’s H2020 (2014-2020/ERC Grant Agreement no. 669416 “LUCKY STAR”). A. Dias-Oliveira thanks the support of the following grants: CAPES (BEX 9110/12-7) FAPERJ/PAPDRJ (E-45/2013). R. Leiva acknowledges support from CONICYT-PCHA/Doctorado Nacional/2014-21141198. R. Duffard, J. L. Ortiz and P. Santos-Sanz have received funding from the European Union’s Horizon 2020 Research and Innovation Programme, under Grant Agreement no 687378. R. Vieira-Martins thanks the following grants: CNPq-306885/2013,

Capes/Cofecub-2506/2015, Faperj: PAPDRJ-45/2013 and E-26/203.026/2015. M. Assafin thanks the CNPq (Grants 473002/2013-2 and 308721/2011-0) and FAPERJ (Grant E-26/111.488/2013). J. I. B. Camargo acknowledges a CNPq/PQ2 fellowship 308489/2013-6. This work has made use of data obtained at the Thai National Observatory on Doi Inthanon, operated by NARIT. A. Maury acknowledges the use of the C. Harlinton telescope of the Searchlight Observatory Network Funding from Spanish grant AYA-2014-56637-C2-1-P is acknowledged, as is the Proyecto de Excelencia de la Junta de Andaluca, J. A. 2012-FQM1776. A. Thirouin acknowledges funding from Lowell Observatory. G.B.R. is thankful for the support of the CAPES (203.173/2016) and FAPERJ/PAPDRJ (E26/200.464/2015 - 227833) grants.

REFERENCES

- Alvarez-Candal, A., Ortiz, J. L., Morales, N. et al. 2014, *Astronomy and Astrophysics*, 571, 48
- Assafin, M., Camargo, J. I. B., Vieira Martins, R. et al. 2010, *Astronomy and Astrophysics*, 515, 32
- Assafin, M., Vieira Martins, R., Camargo, J. I. B. et al. 2011. Gaia FUN-SSO workshop proceedings, 85-88.
- Assafin, M., Camargo, J. I. B., Vieira Martins, R. et al. 2012, *Astronomy and Astrophysics*, 541, 142
- Barkume, K.M., Brown, M.E., Schaller, E.L., 2008. *The Astronomical Journal* **135**, 55–67.
- Barucci, M.A., Alvarez-Candal, A., Merlin, F., Belskaya, I.N., de Bergh, C., Perna, D., DeMeo, F., Fornasier, S., 2011. *Icarus* **214**, 297–307.
- Benedetti-Rossi, G., Sicardy, B., Buie, M.W., Ortiz, J.L. et al., 2016. *The Astronomical Journal*, 152, 156.
- Binzel, R., Farinella, P., V and Cellino, A., 1989. Asteroid rotation rates: distributions and statistics. *Asteroids II* **416**.
- Braga-Ribas, F., Sicardy, B., Colas, F. et al. 2011. Stellar Occultation by Transneptunian Object (208996) 2003 AZ84. Central Bureau Electronic Telegrams **2675**.
- Braga Ribas, F., Sicardy, B., Ortiz, J. L. et al. 2012 AAS/Division for Planetary Sciences Meeting Abstracts, vol. 44, 402.01
- Braga-Ribas, F., Sicardy, B., Ortiz, J. L. et al. 2013, *The Astrophysical Journal*, 773, 26
- Braga-Ribas, F., Sicardy, B., Ortiz, J. L. et al. 2014a, *Nature*, 508, 72-75
- Braga-Ribas, F.; Vieira-Martins, R.; Assafin, M. et al. 2014b, *RevMexAA*, 44, 3-3
- Brown, M.E., Suer, T.A., 2007. Satellites of 2003 AZ₈₄, (50000), (55637), and (90482). *IAU circ.* **8812**.
- Buie, M.W., Keller, J.M., 2016. *The Astrophysical Journal* **151**, 73.
- Burns, Joseph A.; Safronov, V. S., 1973. *MNRAS* **165**, 403.
- Camargo, J. I. B., Vieira-Martins, R., Assafin, M. et al. 2014, *Astronomy and Astrophysics*, 561, 37
- Chandrasekhar, S., *Ellipsoidal figures of equilibrium* 1987.
- Desmars, J., Camargo, J. I. B., Braga-Ribas, F. et al. 2015, *Astronomy and Astrophysics*, 584, A96

- Duffard, R., Ortiz, J.L., Thirouin, A. et al. 2009. *Astronomy and Astrophysics* **505**, 1283–1295.
- Elliot, J. L., Person, M. J., Zuluaga, C. A. et al. 2010, *Nature*, 465, 897
- Goldstein, H. 1950, Addison -Wesley
- Guilbert, A., Alvarez-Candal, A., Merlin, F. et al. 2009. *Icarus* **201**, 272–283.
- Lacerda, P. & Jewitt, D.C. 2007, *The Astronomical Journal*, 133, 1393.
- Lykawka, P. S. & Mukai, T. 2008, *The Astronomical Journal*, 135, 1161.
- Marsden, B. G. 2009, *Minor Planet Electronic Circulars*, 2009-P26.
- Mommert, M., Harris, A.W., Kiss, C. et al. 2012. *Astronomy and Astrophysics* **541**, A93.
- Mueller, T.G., 2015. *IAU General Assembly* **22**, 2256607.
- Nimmo, F., Umurhan, O.M., Lisse, C.M. et al. *ArXiv e-prints*.
- Ortiz, J. L., Sicardy, B., Braga-Ribas, F. et al. 2012 *Nature*, 491, 5660
- Ortiz, J.L., Gutiérrez, P.J., Santos-Sanz, P. et al. 2006. *Astronomy and Astrophysics* **447**, 1131–1144.
- Ortiz, J. L., Duffard, R., Pinilla-Alonso, N. et al. 2015, *Astronomy and Astrophysics*, 576, 180
- Perna, D., Barucci, M.A., Fornasier, S. et al. 2010. *Astronomy and Astrophysics* **510**, A53.
- Person, M. J., Elliot, J. L., Bosh, A. S. et al. 2011, *American Astronomical Society Meeting Abstracts #218*, 224.12
- Plummer, H.C., 1919. *MNRAS* **80**, 26.
- Ruprecht, J. D., Bosh, A. S., Person, M. J. et al. 2015. *Icarus*, 252, 271-276.
- Quillen, A.C., Giannella, D., Shaw, J.G., Ebinger, C., 2016. *Icarus* **275**, 267–280.
- Sallum, S., Brothers, T., Elliot, J. L. et al. 2011, *American Astronomical Society Meeting Abstracts #218*, 224.13
- Santos-Sanz, P., Ortiz, J.L., Barrera, L. et al. 2009. *Astronomy and Astrophysics* **494**, 693–706.
- Sheppard, S.S., Jewitt, D.C., 2003. *Hawaii Kuiper Belt Variability Project: An Update. Earth Moon and Planets* **92**, 207–219.
- Sicardy, B. Colas, F., Maquet, L. et al. 2010, *AAS/Division for Planetary Sciences Meeting Abstracts #42*, 993
- Sicardy, B., Ortiz, J. L., Assafin, M. et al. 2011, *Nature*, 478, 493-496
- Stansberry, J., Grundy, W., Brown, M. et al. 2008, in *The Solar System Beyond Neptune*, p.p. 161-179
- Stern, S.A., Bagenal, F., Ennico, K. et al. *Science* **350**, aad1815.
- Tancredi, G. & Favre, S. 2008, *Icarus*, 195, 851
- Thirouin, A., Ortiz, J.L., Duffard, R. et al. 2010. *Astronomy and Astrophysics* **522**, A93.

- Thirouin, A., Sheppard, S.S., Noll, K.S. et al. 2016. *The Astronomical Journal* **151**, 148.
- Trujillo, C. A.; Brown, M. E.; Helin, E. F. et al. 2003, *Minor Planet Electronic Circulars*, 2003-B27
- Vachier, F., Berthier, J., Marchis, F. AAS/Division for Planetary Sciences Meeting Abstracts vol. 44 of *AAS/Division for Planetary Sciences Meeting Abstracts 2012* p. 111.09.
- van Belle, G. T. 1999, *Publications for the ASP*, 111, 1515
- Widemann, T., Sicardy, B., Dusser, R. et al. 2009, *Icarus* 199, 458-476
- Zacharias, N., Monet, D. G., Levine, S. E. et al. 2004, *American Astronomical Society Meeting Abstracts*, vol. 36, 1418 *Icarus* **228**, 301–314.

Table 1. Astrometric observations for the 2012 event prediction.

Site IAU code	Date mm/dd/yyyy	Telescope
Pico dos Dias Observatory 874	09/22/2011	0.60 m Boller & Chivens
La Hita Observatory I95	01/18/2012 to 01/20/2012	0.77 m
San Pedro de Atacama Observatory ¹ I16	01/16/2012 to 01/25/2012	0.4 m IAA-ASH2
Observatorio Astronomico de Cala d'Hort C85	01/16/2012 to 01/25/2012 ²	0.5 m
Pic du Midi Observatory ¹ 586	01/17/2012	1.0 m

¹ The star and TNO were observed in the same field of view, allowing for the correction in their relative position. ² Data obtained in two nights in this range.

Table 2. Observation circumstances for the February 3, 2012 event.

Site	Longitude (W) Latitude (N) Altitude (m)	Telescope Camera	Expo. Time Cycle (s)	Observer	Detection
Mt. Abu (India)	-72° 46' 47.18" 24° 39' 10.34" 1680	1.2 m NICMOS	4.0 4.98	T. Baug, Jinesh Jain T.Chandrasekhar S. Ganesh	positive
IUCAA ¹ Girawali (IGO) (India)	-73° 40' 00.0" 19° 05' 00.0" 1005	2.0 m IFOSC	2.0 16.5	V. Mohan	positive
Kraar (Israel)	-34° 48' 45.76" 31° 54' 29.1" 107	0.41 m SBIG ST-8XME CCD	3.0 4.4-5.0?	I. Manulis E. Ofek A. Gal-Yam	positive
Liverpool Tel. Canary (Spain)	17° 52' 45.2" 28° 45' 48.8" 2457	2.00 m RISE	1.5 1.5	Robotic Telescope	negative
Wise (Israel)	-34° 45' 48.0" 30° 35' 45.0" 875	1.00 m Princeton Instrument CCD	3.0 4.5	S. Kaspi N. Brosch	Clouded
Nikaya Observatory (India)	-77° 43' 33.0" 12° 36' 23.0" 1005	0.36 m SBIG ST-8XME CCD	4.0 6.2	A. A. Sharma	negative
Maidenhead (United Kingdom)	-00° 48' 58.2" 51° 30' 23.8" 75	0.30 m WATEC 120N+	2.56 2.56	T. Haymes	negative
Paris Observatori - Mobile Station - (France)	01° 50' 19.9" 46° 31' 08.2" 305	0.21 m WATEC 120N+	2.56 2.56	J. Lecacheux	negative
Cabrills (Spain)	02° 23' 07.3" 41° 31' 11.3" 114	0.30 m SBIG ST8-XME	10 13	R. Naves	negative
Alicante (Spain)	-359° 33' 18.0" 38° 28' 33.0" 187.3	0.30 m SBIG ST8-XME bin 3x3	3.0 5.0	R. G. Lozano	negative
Tourrette Levens (France)	07° 15' 47.2" 43° 47' 22.2" 385	0.335 m Apogee Alta U1 CCD	5.0 5.68	P. Tanga	negative
Bellinzona (Switzerland)	09° 01' 26.5" 46° 13' 53.2" 260	0.40 m SBIG ST8 CCD	5.0 7.0	S. Sposetti	negative
Berlin (Germany)	13° 28' 30.8" 52° 29' 12.5" 41	0.50 m WATEC 120N	1.28-2.56 1.28-2.56	G. Wortmann	negative
Berlin (Germany)	13° 39' 41.5" 52° 24' 35.4" 45	0.28 m MINTRON 12V6	1.28 1.28	S. Andersson	negative
Nonndorf (Austria)	15° 14' 08.7" 48° 47' 13.5" 593	0.254 m Watec 120N	2.56 2.56	G. Dangl	negative

¹ Inter-University Centre for Astronomy and Astrophysics

Table 3. Observation circumstances for November 15, 2014 event.

Site	Longitude (W) Latitude (N) Altitude (m)	Telescope Camera	Expo. Time Cycle (s)	Observer	Detection
Thai National Telescope (Thailand)	-98° 25' 56.06" 18° 34' 25.41" 2457	2.4 m ULTRASPEC	0.786187 0.801169	A. Richichi P. Irawati	positive
Yunnan (China)	-100° 01' 51.0" 26° 42' 32.0" 3193	2.4 m 1340×1300 CCD Camera	3.0 4.3164	Z. Liying Q. Shengbang Z. Ergang	positive
Moriyama (Japan) CCD	-135° 59' 23.8" 35° 02' 59.1" 105	0.26 m Apogee ALTA U6	10.0 11.65	Y. Ikari	positive
Moriyama (Japan) Video		0.254 WAT-120(slow shutter 256Fr)	08.53 08.53	Y. Ikari	positive
Inabe (Japan)	-136° 31' 24.7" 35° 10' 14.7" 187	0.35 TGV-M (slow shutter 256Fr)	08.53 08.53	A. Asai Hayato Watanabe	Observation finished before actual event
Hamamatsu (Japan) Video	-137° 44' 23.0" 34° 43' 070" 17	0.254 WAT-120(slow shutter 256Fr)	08.53 08.53	M. Owada	negative
Tarui (Japan) Video	-136° 29' 43.7" 35° 23' 41.4" 105	0.35 TGV-M(Slow shutter 64Fr)	2.13 2.13	Hiroyuki Watanabe	Observation finished before actual event
Hitachi (Japan) Video	-140° 41' 08.9" 36° 38' 33.2" 33	0.30 WAT-120N+RC (slow shutter 128Fr)	4.27 4.27	H. Tomioka	Obs. Taken on wrong area
Maibara (Japan) Video	-136° 17' 40.3" 35° 19' 41.8" 92	0.13 WAT-910HX(slow shutter 128Fr)	4.27 4.27	H. Yamamura	Observation finished before actual event

Table 4. Ingress and Egress times.

January 8, 2011				
Site	Ingress (UT)	Error (s)	Egress (UT)	Error (s)
San Pedro Atacama (SPACE)	06:29:48.30	0.80	06:30:10.00	0.8
February 3, 2012				
Mt. Abu	19:45:13.89	0.70	19:45:35.95	2.5
Kraar	19:47:39.20	0.70	19:48:06.15	0.68
IUCAA Girawali	19:45:17.16 ¹	7.3	19:45:25.43	0.10
December 2, 2013				
Rockhampton	14:52:48.44	1.40	14:53:28.17	1.0
November 15, 2014				
Thai National Telescope	17:58:09.57	0.02	17:59:13.80	$\begin{smallmatrix} +0.04 \\ -0.03 \end{smallmatrix}$
Yunnan	17:57:21.65	0.13	17:57:36.95	$\begin{smallmatrix} +0.13 \\ -0.14 \end{smallmatrix}$
Moriyama (CCD)	17:52:15.32	0.18	17:52:59.90	0.20
Moriyama (Video)	17:52:15.25	$\begin{smallmatrix} +3.24 \\ -3.99 \end{smallmatrix}$	17:52:55.69	$\begin{smallmatrix} +4.40 \\ -4.01 \end{smallmatrix}$

¹ Whereas the ingress must happen between 19:45:09.88 and 19:45:24.43 UTC, it can be represented by the mid-time between them with the error being the difference between the two extremes and the midpoint.

Table 5. Physical parameters for 2003 AZ₈₄ from the 2012 and 2014 multi-chord events.

Solution	2012	2014
Apparent semi-major axis a' (km)	426^{+26}_{-16}	393 ± 1
Equivalent radius R_e (km)	346 ± 6	382 ± 3
Projected oblateness ϵ'	$0.340^{+0.097}_{-0.086}$	0.054 ± 0.003
f_c (km) ¹	6800^{+23}_{-17}	$2862^{+2.1}_{-1.8}$
g_c (km) ¹	2850^{+14}_{-11}	$336^{+4.0}_{-2.7}$
Position angle of the limb P_L (deg)	41^{+8}_{-5}	36 ± 4
χ^2_{pdf}	0.73	0.98
Jacobi solution		
Semi-major axis a (km)	470 ± 20	
Axis ratios	$b/a = 0.82 \pm 0.05, c/a = 0.52 \pm 0.02$	
Density ρ (g cm ⁻³)	0.87 ± 0.01	
Visible geometric albedo p_V	0.097 ± 0.009	

¹ The quantities (f_c, g_c) are the offsets, expressed in km, in right ascension ($\Delta\alpha \cos(\delta)$) and declination ($\Delta\delta$) to be applied to 2003 AZ₈₄'s ephemeris (NIMA V1), as deduced from the elliptical fits to the chord extremities shown in Figs. 6 and 7, using the star positions of Eqs. 2 and 3. The NIMA ephemeris provides the following reference J2000 geocentric positions for the body: (07^h45^m54.79070^s, +11°12'43.0422'') and heliocentric distance $\Delta = 6.6209 \times 10^9$ km on February 3, 2012 at 19:45 UTC, and (08^h03^m51.28512^s, +09°57'18.7956''), $\Delta = 6.6634 \times 10^9$ km on November 15, 2014 at 17:55 UTC. Applying the (f_c, g_c) offsets tabulated here, we obtain the following corrected geocentric positions for 2003 AZ₈₄: (07^h45^m54.80510^s, +11°12'43.1310'') and (08^h03^m51.29112^s, +09°57'18.8060'') at each date, respectively. Those positions are independent of the ephemeris, but depend on the assumed star positions (Eqs. 2 and 3).

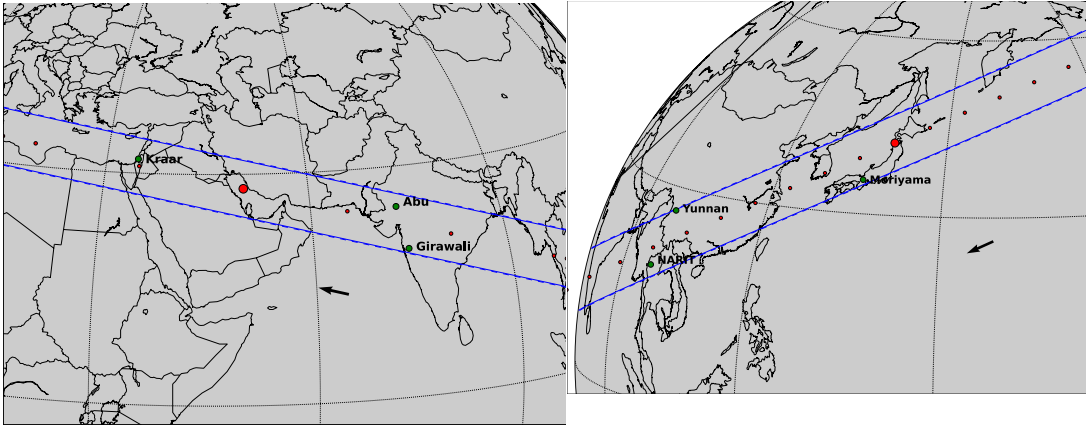


Fig. 1.— The shadow paths of the two multi-chord events analyzed here (February 3, 2012 at left and November 15, 2014 at right), the blue solid lines corresponding to the approximate size of the object. The smaller red dots mark the shadow center every minute, while the larger dot indicates the time of closest approach to the geocenter. The arrows show the direction of motion. The green dots mark the sites where data were obtained with positive detection of the event.

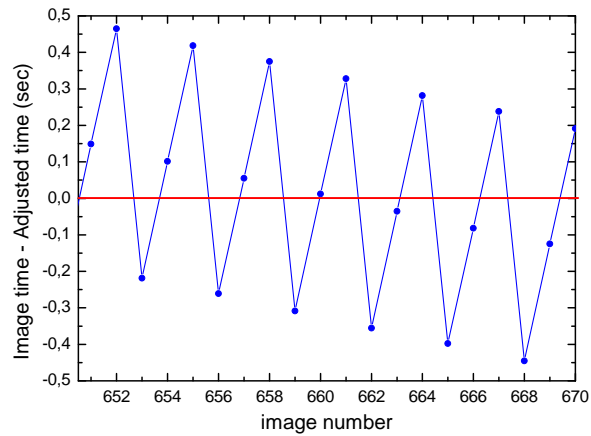


Fig. 2.— Example of the saw pattern obtained with the residuals of the linear fit (blue line) of the truncated time. For this kind of fit we used points around the event, during a period in which the acquisition was regular.

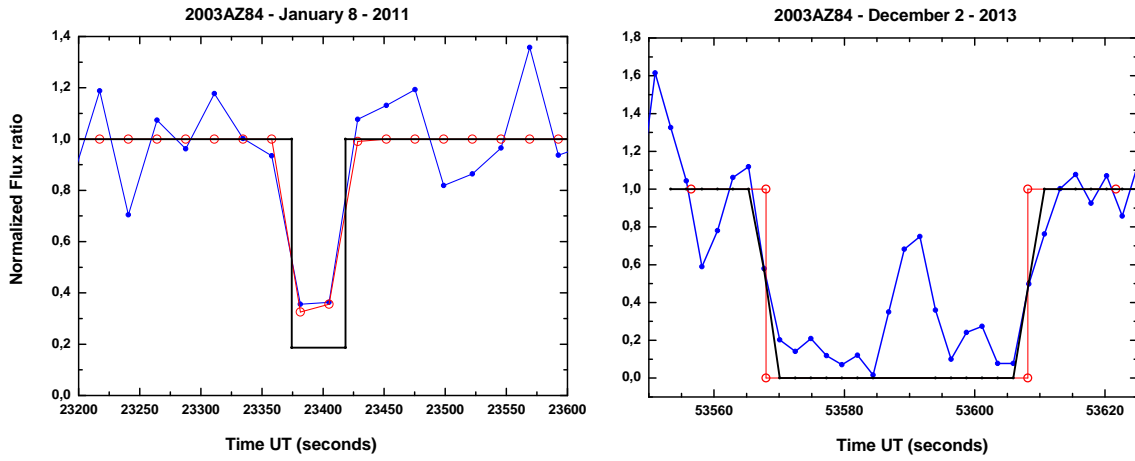


Fig. 3.— Fits to the single-chord events of January 8, 2011 (left panel) and December 2, 2013 events (right panel). In both panels, the blue lines and dots are the observed occultation light curve plotted vs. time. The solid black lines show the square-well models that best fit the data, while the red lines and circles show the synthetic flux after convolution of the square-well models by Fresnel diffraction, star angular diameter projected at the body and finite exposure time, see Section 3.2 for details.

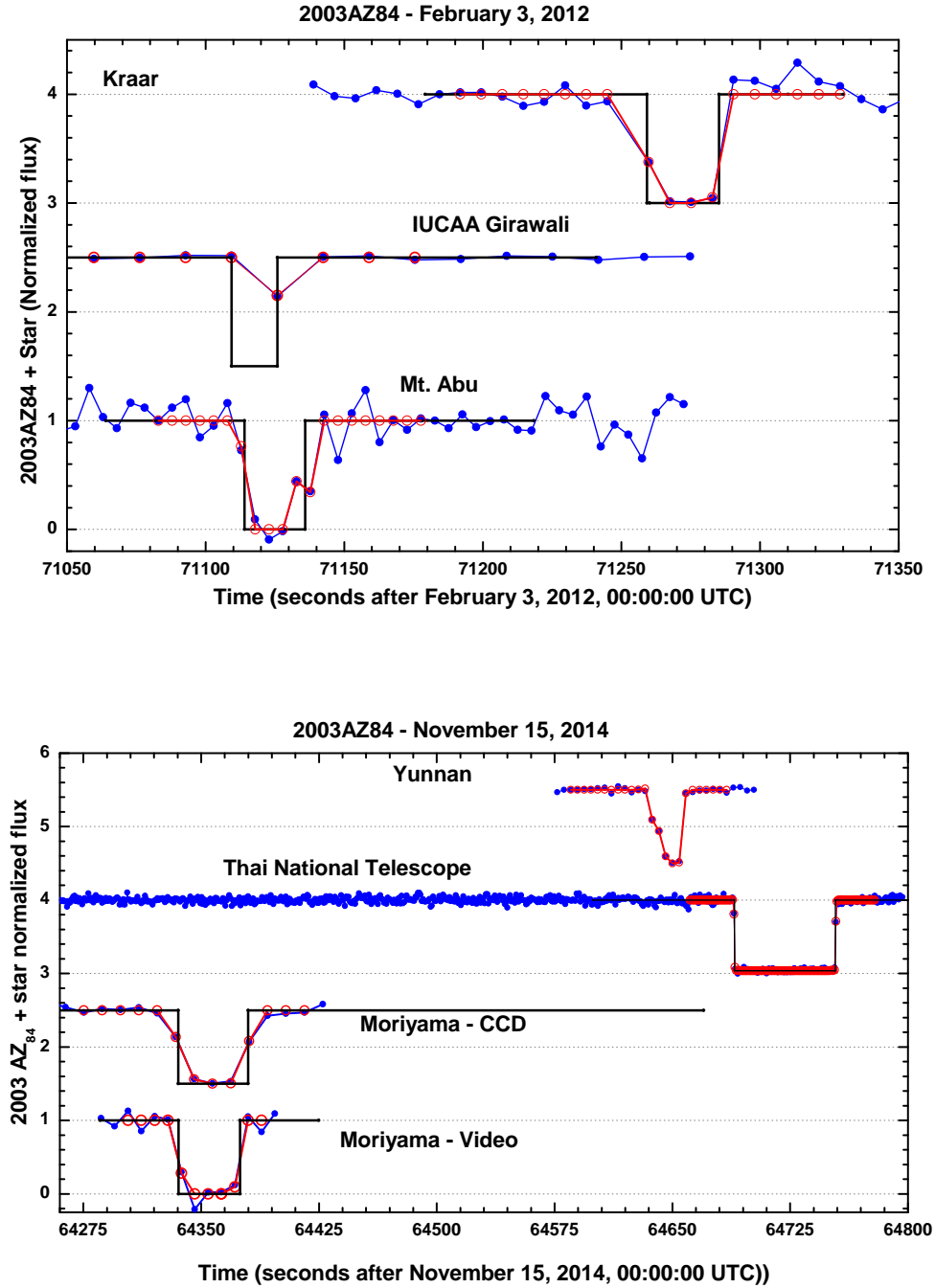


Fig. 4.— Same conventions as for the previous figure. Top panel: the four occultation light curves obtained during the 2014 event, vertically shifted for better viewing. Bottom panel: same as top panel for the three light curves obtained during the 2012 event.

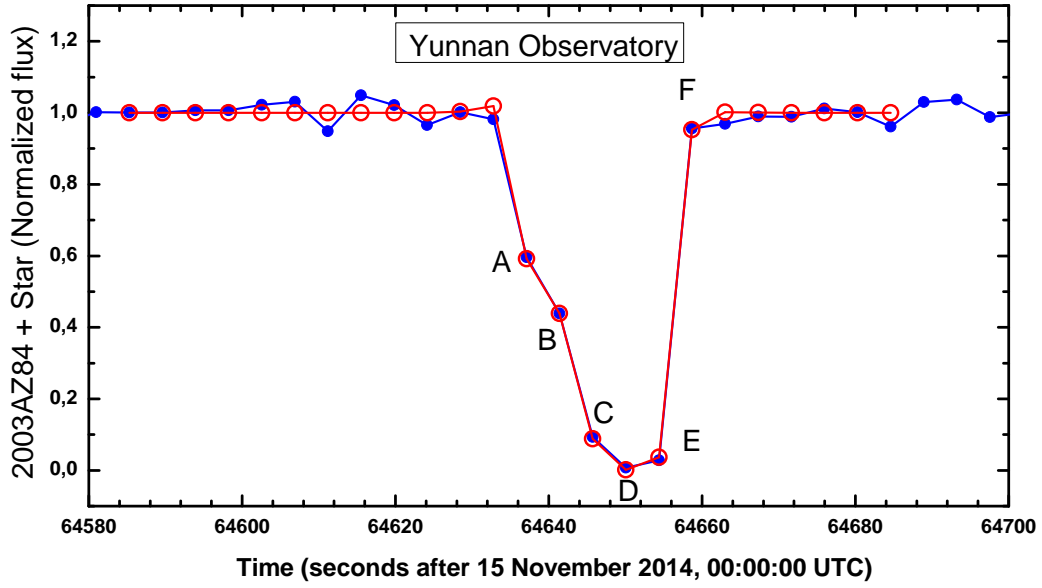


Fig. 5.— Expanded view of the Yunnan light curve shown in Fig. 4, showing the gradual drop at ingress. The model (red lines and circles) has been generated using the two possible topographic solutions displayed in Fig. 13 (providing identical fit to the data).

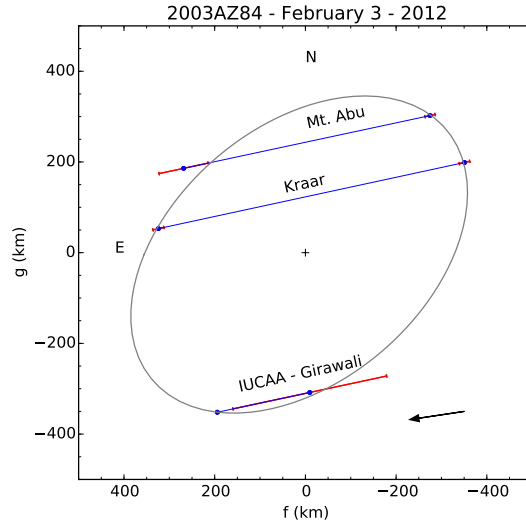


Fig. 6.— Blue lines: the occultation chords showing the stellar motion (from right to left, see arrow) relative to 2003 AZ₈₄'s fitted center, as observed from the three station of February 3, 2012. The red segments indicate the 1- σ error bars on each chord extremity, derived from the time uncertainties provided in Table 4. Here, the star offsets (f , g) in right ascension and declination, respectively, have their origin arbitrarily fixed at the body fitted center (cross) and are expressed in kilometers. Black line: the best elliptical limb fit, whose geometric parameters are listed in Table 5. Label N (resp. E) indicates local celestial north (resp. east). Besides the chords shown here, no secondary events were detected, as could be caused by satellites or rings.

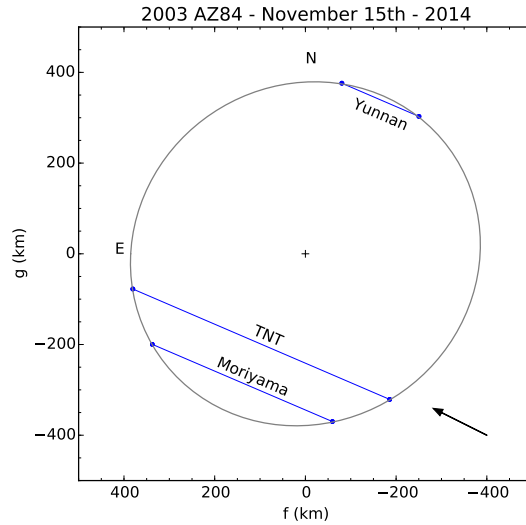


Fig. 7.— Same as Figure 6, but for the November 15, 2014 event.

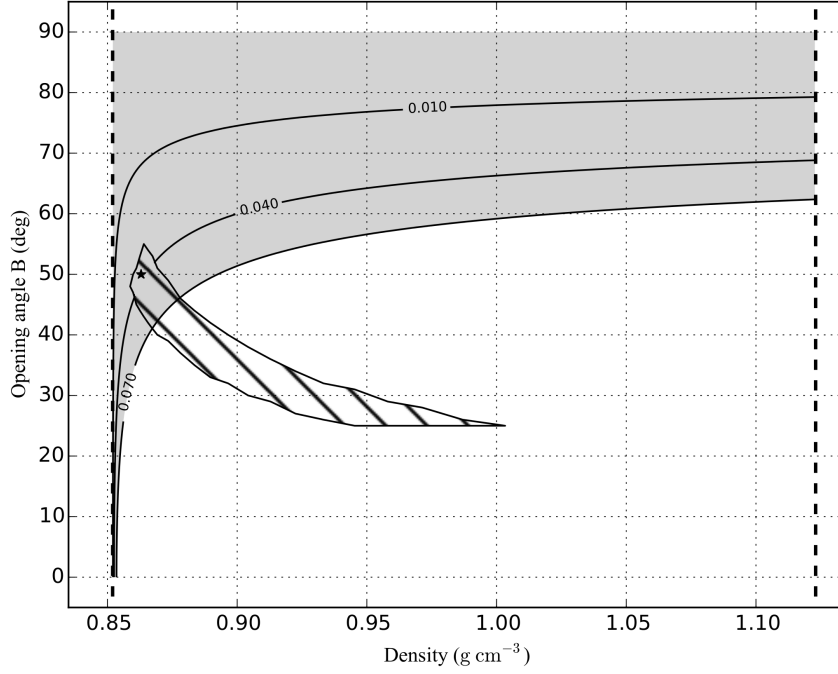


Fig. 8.— The hatched band shows the range ($1\text{-}\sigma$ level) of possible opening angles B ($B = 0^\circ$ and $B = 90^\circ$ corresponding to equator-on and pole-on orientations, respectively) as a function of density for a Jacobi ellipsoid with rotation period $P = 6.75$ h, using the limb solutions shown in Figs. 6 and 7. **The dashed vertical lines at $\rho = 0.853$ and $\rho = 1.12 \text{ g cm}^{-3}$** are the theoretical limits for the Jacobi solutions. The solid black lines are the loci of constant rotational light curve amplitude ($\Delta m = 0.01, 0.04, 0.07$ mag) for a Jacobi ellipsoid, using Eq. 5 of Binzel et al. (1989). The shaded region correspond to the constraint $\Delta m < 0.07$ provided by observations, see text. The intersection of the band with the shaded region provides a density $\rho \sim 0.87 \pm 0.01 \text{ g cm}^{-3}$ and opening angle $B \sim 48^\circ \pm 7^\circ$. The star symbol defines the solution illustrated in Fig. 9.

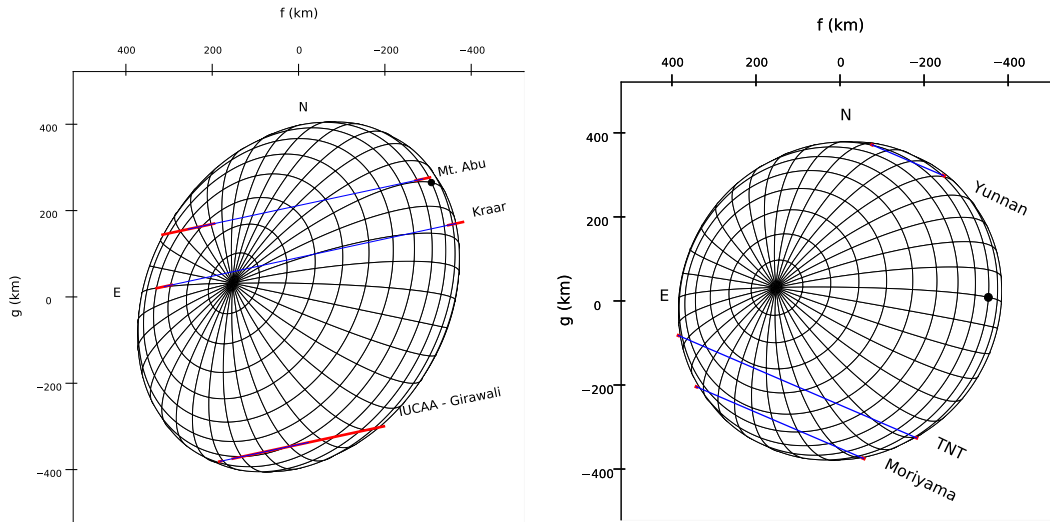


Fig. 9.— A possible Jacobi ellipsoid solution that fits both 2012 and 2014 occultation results. It has semi-major axes $a \times b \times c = 456 \times 382 \times 242$ km, opening angle $B = 50^\circ$ and density $\rho = 0.86 \text{ g cm}^{-3}$, corresponding to the dot in Fig. 8. The **position angle of the pole** is $P_p = 78^\circ$ (not to be confounded with the **position angle of the limb** P_L , see text). The black dot marks the intersection of the longer axis a with the surface of the body. Left panel: fit to the 2012 event, using a rotation angle $Q = 45^\circ$. Right panel: fit to the 2014 event, using a rotation angle $Q = 10^\circ$. See text for details.

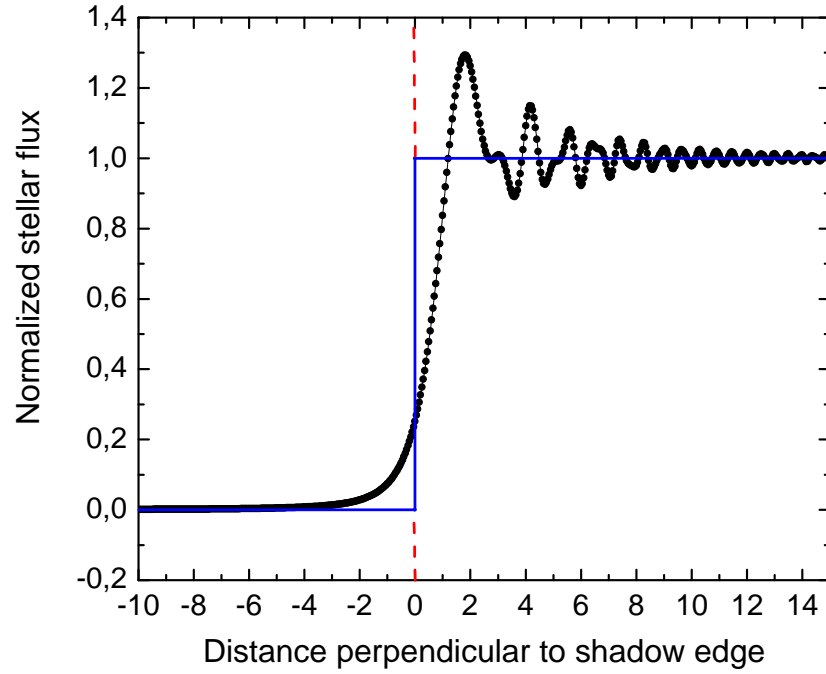


Fig. 10.— Black line and dots: the Fresnel diffraction pattern perpendicular to a shadow edge observed at 6.67×10^9 km (44.5 AU), corresponding to the geocentric distance of 2003 AZ₈₄ on November 15, 2014. The blue line is the abrupt edge profile (located along the red dashed line) that would be obtained in the limit of geometric optics and with a point-like star. Moreover, the pattern has been averaged over a spectral interval of $0.3 \mu\text{m}$ in the visible domain to account for the broadband response of the CCD at the Yunnan station.

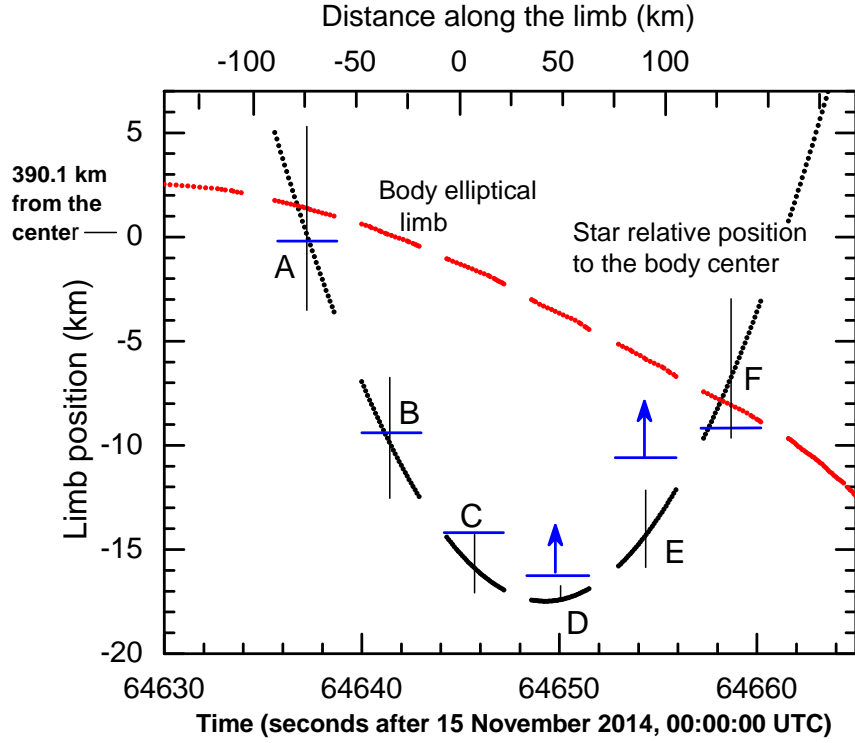


Fig. 11.— Modeling the shallow depression solution (Solution 2 in the text). The black dots along the parabola show the star position relative to 2003 AZ₈₄'s center at 0.1 s time steps, inside each integration interval (solid blue lines). The gaps correspond to the read out time of each image, with no data acquired. The origin of the vertical scale has been chosen arbitrarily so as to correspond to a radial distance of 390.1 km (close to the distance corresponding to the mid-time of interval A) The solid vertical lines are the mid-time of each exposure and the solid red lines are the limb radial distances provided by the global elliptical fit. The vertical position of each blue line marks the limb offset for each acquisition interval that reproduces the observed normalized flux of Fig. 5. The blue arrows on intervals D and E indicate that only a lower limit for the local limb offset could be derived (as no signal from the star was recorded during those intervals). The upper horizontal axis shows the distance traveled by the star relative to the limb, with arbitrary origin corresponding to interval C. See text for more details.

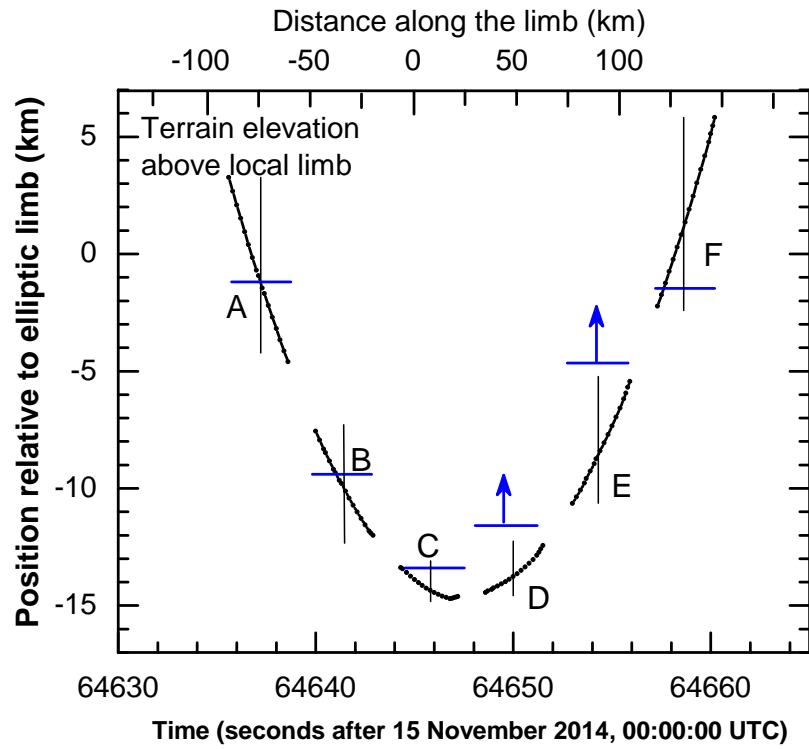


Fig. 12.— Same as Figure 11, but showing the difference in height between the blue lines (and black dots) and the red lines from Figure 11. This provides the average elevation of the terrain in each interval with respect to the global elliptical limb, see also Fig. 13.

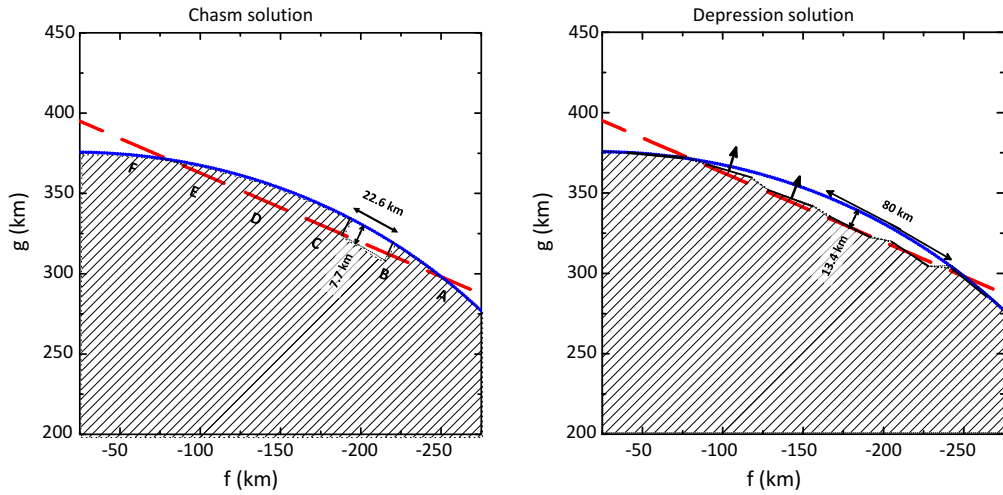


Fig. 13.— Two possible limb solutions that can explain the gradual ingress at the Yunnan site during the November 15, 2014 occultation (Fig. 5). In each panel, the blue line is the global fitted limb (see Fig. 7) and the red segments show the star motion during each exposure interval. Left panel: chasm solution (Solution 1 in the text) with vertical walls. The width of the chasm is 22.6 ± 0.4 km but only a lower limit of 7.7 km for its depth can be derived from the data. Right panel: depression solution (Solution 2). The black segments are the positions of the average limb in each integration interval. The black arrows on segments D and E indicate that they are the deepest possible levels for the limb that can be derived from the data (since the star is not visible during those integration intervals, see Fig. 5). As a consequence, a lower limit for the horizontal extension of the depression is 80 km, while its depth 13.4 km. See text for details.